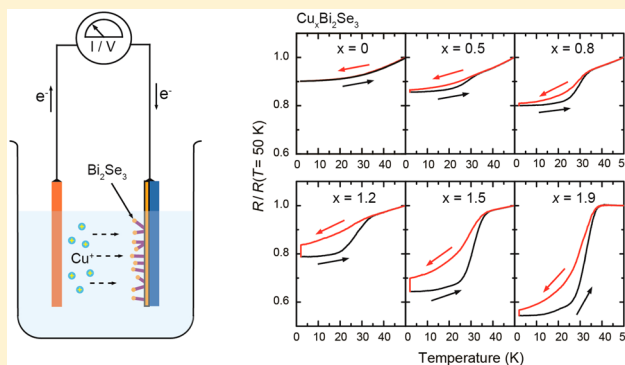


# Electrochemical Control of Copper Intercalation into Nanoscale $\text{Bi}_2\text{Se}_3$

Jinsong Zhang,<sup>†</sup> Jie Sun,<sup>†</sup> Yanbin Li,<sup>†</sup> Feifei Shi,<sup>†</sup> and Yi Cui<sup>\*,†,‡</sup><sup>†</sup>Department of Materials Science and Engineering, Stanford University, Stanford, California 94305, United States<sup>‡</sup>Stanford Institute for Materials and Energy Sciences, SLAC National Accelerator Laboratory, 2575 Sand Hill Road, Menlo Park, California 94025, United States**S** Supporting Information

**ABSTRACT:** Intercalation of exotic atoms or molecules into the layered materials remains an extensively investigated subject in current physics and chemistry. However, traditionally melt-growth and chemical interaction strategies are either limited by insufficiency of intercalant concentrations or destitute of accurate controllability. Here, we have developed a general electrochemical intercalation method to efficaciously regulate the concentration of zerovalent copper atoms into layered  $\text{Bi}_2\text{Se}_3$ , followed by comprehensive experimental characterization and analyses. Up to 57% copper atoms ( $\text{Cu}_{6.7}\text{Bi}_2\text{Se}_3$ ) can be intercalated with no disruption to the host lattice. Meanwhile the unconventional resistance dip accompanied by a hysteresis loop below 40 K, as well as the emergence of new Raman peak in  $\text{Cu}_x\text{Bi}_2\text{Se}_3$ , is a distinct manifestation of the interplay between intercalated Cu atoms with  $\text{Bi}_2\text{Se}_3$  host. Our work demonstrates a new methodology to study fundamentally new and unexpected physical behaviors in intercalated metastable materials.

**KEYWORDS:** Electrochemical intercalation, bismuth selenide, two-dimensional materials, resistance dip, hysteresis



Following graphene, a broad family of two-dimensional (2D) layered materials have attracted intense interest in fundamental research and technological development.<sup>1–5</sup> Among all the efforts to control and improve their properties, intercalation of atomic or molecular guest species into the van der Waals gap of 2D materials represents one of the most promising methods in the low-temperature synthesis strategy for the design and application of solids with particular composition, structure, physical performance, and chemistry reactivity.<sup>6–10</sup> Since conventional crystal growth requires consequently high temperatures close to the melting point of the reactants, the thermodynamics control of molecular reaction becomes dominant in the determination of the structure, concentration, and defects, which is significantly different compared to the kinetically trapped metastable phases.<sup>11</sup>

Tuning the concentration of intercalants has been widely explored to produce dramatic modulations in the field of electronics, photonics, energy storage, catalysis, and multifunctional devices.<sup>12–19</sup> One of the prominent cases is the emergence of topological superconductor by copper intercalation into  $\text{Bi}_2\text{Se}_3$  crystals, which triggers the burst of exploration for Majorana Fermion in condensed matter physics.<sup>20–24</sup> However, nearly all these crystal syntheses employ melt-growth method with the Cu concentration limited to  $x = 0.5$  ( $\text{Cu}_x\text{Bi}_2\text{Se}_3$ ) and cannot avoid the formation of substitu-

tional defects, resulting in hole doping to the system and nonzero valence of Cu atoms. Recently, our group has developed a chemical method to intercalate zerovalent copper into  $\text{Bi}_2\text{Se}_3$  nanoribbons by using low-temperature solution-based disproportionation redox reaction,<sup>25</sup> then further generalized it for more zerovalent metals into other 2D layer nanomaterials.<sup>26–28</sup> Nevertheless, the accurate controllability of  $\text{Cu}^0$  concentration in  $\text{Cu}_x\text{Bi}_2\text{Se}_3$  has not been implemented in practice.

In this work, we employed a more accurate and controllable strategy to electrochemically intercalate zerovalent copper into nanoscale  $\text{Bi}_2\text{Se}_3$  in a battery cell configuration, yielding a high Cu concentration up to  $x = 6.7$ . Moreover, we performed a comprehensive study of the Cu-intercalated nanoscale  $\text{Bi}_2\text{Se}_3$  by means of transmission electron microscopy (TEM) characterization, X-ray diffraction (XRD), X-ray photoelectron spectroscopy (XPS), energy-dispersive X-ray (EDX) spectroscopy, Raman spectroscopy, and low-temperature transport. It is confirmed that the host lattice structure is not disrupted by zerovalent Cu intercalation up to the highest concentration ( $x = 6.7$ ). Most strikingly, low-temperature transport reveals an unconventional resistance dip accompanied by a hysteresis

Received: December 6, 2016

Revised: February 16, 2017

Published: February 20, 2017

behavior below 40 K. In addition, the emergence of new peak in the Raman spectroscopy indicates the formation of new vibration mode due to the interplay between intercalated Cu atoms and host lattice. All of our findings demonstrate a new route to explore Cu-intercalated metastable materials and design unique devices for potential applications.

$\text{Bi}_2\text{Se}_3$  is one of the prototype topological insulators and possesses rhombohedral lattice structure [space group  $D_{3d}^5$  ( $R\bar{3}m$ )] with five atoms in one unit cell.<sup>29–31</sup> The Bi and Se hexagonal planes are close stacked along the  $c$  axis and repeated every five atomic layers as Se(1)–Bi–Se(2)–Bi–Se(1), occupying A–B–C sites alternatively as shown in the inset of Figure 1B. The van der Waals gap is in between two neighboring Se(1) layers with the gap size  $d = 2.6$  Å, larger than the diameter of  $\text{Cu}^+$  (1.8 Å),<sup>32</sup> enabling the intercalation process.

In our electrochemical intercalation setup (Figure 1A), the working electrode (WE) is  $\text{Bi}_2\text{Se}_3$  nanoribbons grown on the conductive palladium/quartz substrates by using the vapor-liquid–solid method (see materials and methods section in

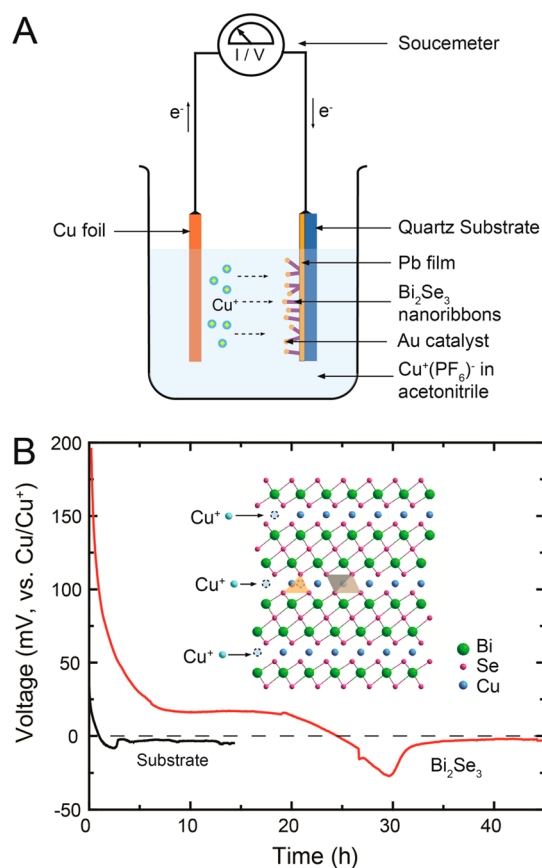


**Figure 1.** Electrochemical intercalation of Cu atoms into  $\text{Bi}_2\text{Se}_3$  nanoribbons. (A) Schematic of our electrochemical intercalation setup. The working electrode is  $\text{Bi}_2\text{Se}_3$  nanoribbons growth on Pb/quartz substrate with Au as the catalyst. Cu foil serves both as the counter electrode and reference electrode. The electrolyte is  $[\text{Cu}(\text{CH}_3\text{CN})_4]\text{PF}_6$  solved in anhydrous acetonitrile. The source meter is used to apply the constant current and record voltage. (B) The voltage profiles of working electrode for  $\text{Bi}_2\text{Se}_3$  nanoribbons (red line) and Au/Pd/quartz substrate (black line), respectively. Inset: hypothetical sketch of  $\text{Cu}^+$  intercalation into  $\text{Bi}_2\text{Se}_3$  host lattice; the octahedron and tetrahedron of Se atoms are indicated by gray and yellow colors.

Supporting Information). Meanwhile, a bare Cu film is used both as the counter (CE) and reference electrode (RE). The electrolyte is 10 mM  $[(\text{CH}_3\text{CN})_4\text{Cu}]\text{PF}_6$  in acetonitrile. Between WE and CE, we applied a small 10 nA current for minimizing the ohmic loss in the electrolyte to drive  $\text{Cu}^+$  ion intercalation into  $\text{Bi}_2\text{Se}_3$  nanoribbons on the WE. As shown in the red curve of Figure 1B, the voltage of  $\text{Bi}_2\text{Se}_3$  WE relative to RE has two well-defined plateaus located at 17 and  $-3$  mV, respectively. When  $\text{Bi}_2\text{Se}_3$  WE is replaced by the bare Au/Pd/quartz substrate without  $\text{Bi}_2\text{Se}_3$  materials, only the lower plateau at  $-3$  mV can be observed. These results indicate that the lower plateau is related to Cu metal deposition onto WE, and the higher one at 17 mV is a consequence of Cu intercalation into  $\text{Bi}_2\text{Se}_3$  nanoribbons (see more discussion in Supporting Information). Thus, we can describe the electrochemical reaction as the following oxidation and reduction formulas:  $\text{Bi}_2\text{Se}_3 + x\text{Cu}^+ + xe^- \rightarrow \text{Cu}_x\text{Bi}_2\text{Se}_3$  on the WE side;  $x\text{Cu} \rightarrow x\text{Cu}^+ + xe^-$  on the CE side. To tune the Cu concentration in  $\text{Bi}_2\text{Se}_3$  nanoribbons, we controlled the electrochemical reaction time at a given current and maintained WE voltage always larger than 0 V to avoid Cu metal deposition.

After electrochemical intercalation, the properties of Cu-intercalated nanoscale  $\text{Bi}_2\text{Se}_3$  are studied by a series of characterization methods, including TEM, XRD, XPS, EDX, Raman spectroscopy, and low-temperature transport. As shown in Figure 2A, electron diffraction of pristine  $\text{Bi}_2\text{Se}_3$  nanoribbon along the  $c$ -axis represents a prototypical hexagonal pattern of single crystal, which is further confirmed by high-resolution TEM image (Figure 2D). No observable change in the diffraction pattern can be detected as long as the Cu concentration  $x < 0.5$ . However, when  $x$  increased to 1.4, we found a tremendous intensity modulation with alternating dark and bright diffraction spots at  $\{11\bar{2}0\}$  and  $\{3\bar{3}00\}$  sites, respectively (Figure 2B). Meanwhile, the overall characteristic hexagonal diffraction pattern remains unchanged, suggesting a stable host lattice and absence of secondary phases, such as Cu precipitates,  $\text{Cu}_2\text{Se}$ , and  $\text{CuSe}$ . This diffraction pattern has been previously reported by Koski et al. in Sn and Ni intercalated  $\text{Bi}_2\text{Se}_3$  nanoribbons by means of chemical reaction.<sup>26</sup> As  $x$  is further increased to  $x = 6.7$ , besides the intensity alternation in the diffraction pattern, each of the host lattice spots is surrounded by six hexagonal superlattice spots (Figure 2C). Actually, these superlattice spots are the family of  $\{1100\}$  spots that are normally forbidden in the rhombohedral  $\text{Bi}_2\text{Se}_3$  host lattice. Refer to previous work reported by Koski et al.,<sup>25</sup> the intensity alternation and absence of  $\{\frac{1}{2}\frac{1}{2}\bar{1}0\}$  superlattice spots (the midpoint of adjacent host lattice spots) in our results are two remarkable differences compared with chemical intercalated  $\text{Cu}_x\text{Bi}_2\text{Se}_3$ .

For the pristine  $\text{Bi}_2\text{Se}_3$ , the high-resolution TEM image viewed from the  $c$ -axis direction (Figure 2D) shows a uniform hexagonal lattice with the  $\{11\bar{2}0\}$  interplanar distance at  $d_0 = 2.07$  Å. When Cu atoms are intercalated into  $\text{Bi}_2\text{Se}_3$  frame, a fringe- or puddle-like moiré patterns were detected with separation of each fringe  $\sim 2.5$  nm (Figure 2E,F). Since moiré patterns generally happen in specimens consisting of two similar thin films superimposed with a small lattice difference, there should be a lattice mismatch due to the Cu intercalation in a single nanoribbon. By comparing the intensity profiles along  $(3\bar{3}00)$  and  $(\bar{3}300)$  in the diffraction pattern between Figure 2A,C (Figure S5), we found extra shallow points next to

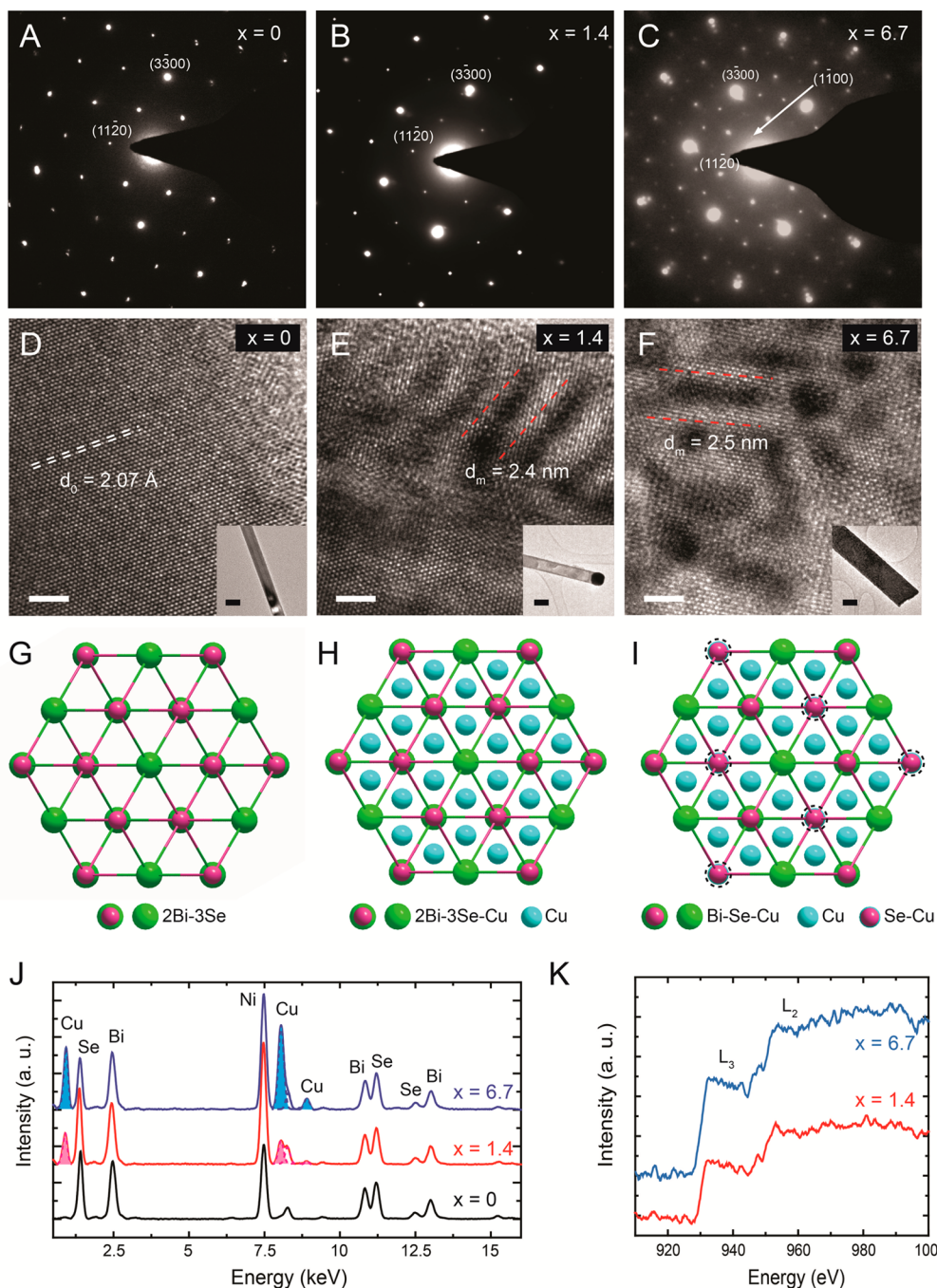


**Figure 2.** TEM characterization of Cu intercalated  $\text{Bi}_2\text{Se}_3$  nanoribbons. (A–C) The electron diffraction pattern of  $\text{Cu}_x\text{Bi}_2\text{Se}_3$  for  $x = 0, 1.4,$  and  $6.7,$  respectively. Comparing with uniform hexagonal pattern for pristine  $\text{Bi}_2\text{Se}_3$  (A), an intensity modulation with dark and bright diffraction spots at  $\{11\bar{2}0\}$  and  $\{3\bar{3}00\}$  sites was detected for  $x = 1.4$  (B). The family of  $\{1\bar{1}00\}$  diffraction spots were observed in (C) for  $x = 6.7$ . (D–F) High-resolution TEM images for  $x = 0, 1.4,$  and  $6.7$ . The scale bare (white) is 2 nm. The insets map the morphology of each nanoribbon with a 200 nm scale bare (black). The separation of  $\{11\bar{2}0\}$  faces is indicated as  $d_0 = 2.07 \text{ \AA}$ . Moiré fringes were presented in (E) and (F) with the distance  $d_m \approx 2.5 \text{ nm}$ . (G–I) Simulated lattice structures that produce similar diffraction patterns shown in (A–C). Viewed from  $c$  direction, each hexagonal site is a representative of a series of atoms with defined ratios as labeled in the bottom. In (I), due to the interplanar restacking, Bi atoms are missing in C sites as indicated by dashed circles. (J) Normalized TEM-EDX spectra of these three  $\text{Bi}_2\text{Se}_3$  nanoribbons. The copper contributions are fitted and highlighted by solid colors. Ni peaks are from TEM grids. (K) The EELS fine structures reveal that the intercalated Cu atoms are in zerovalent.

$\text{Bi}_2\text{Se}_3$   $\{3\bar{3}00\}$  spots for the  $x = 6.7$  sample, indicating the expansion of  $\{11\bar{2}0\}$  interplanar layers with the distance increased to  $d_1 = 2.23 \text{ \AA}$ . Therefore, the separation of each moiré fringe can be calculated,  $d_m = d_0^2/(d_1 - d_0) = 2.67 \text{ nm}$ , which is consistent with that shown in TEM images. All these findings remind us that Cu concentration may not be uniform everywhere within a single nanoribbon, the outer layers and/or

the edges may have higher Cu concentrations and resulting lattice expansion.

Figure 2G shows the top view of  $\text{Bi}_2\text{Se}_3$  host lattice, each hexagonal spot is representative of two Bi and three Se atoms. They have equal scattering weight to electron beam and thus produce a uniform hexagonal diffraction pattern, as that shown in Figure 2A. If Cu atoms are intercalated into the host lattice,

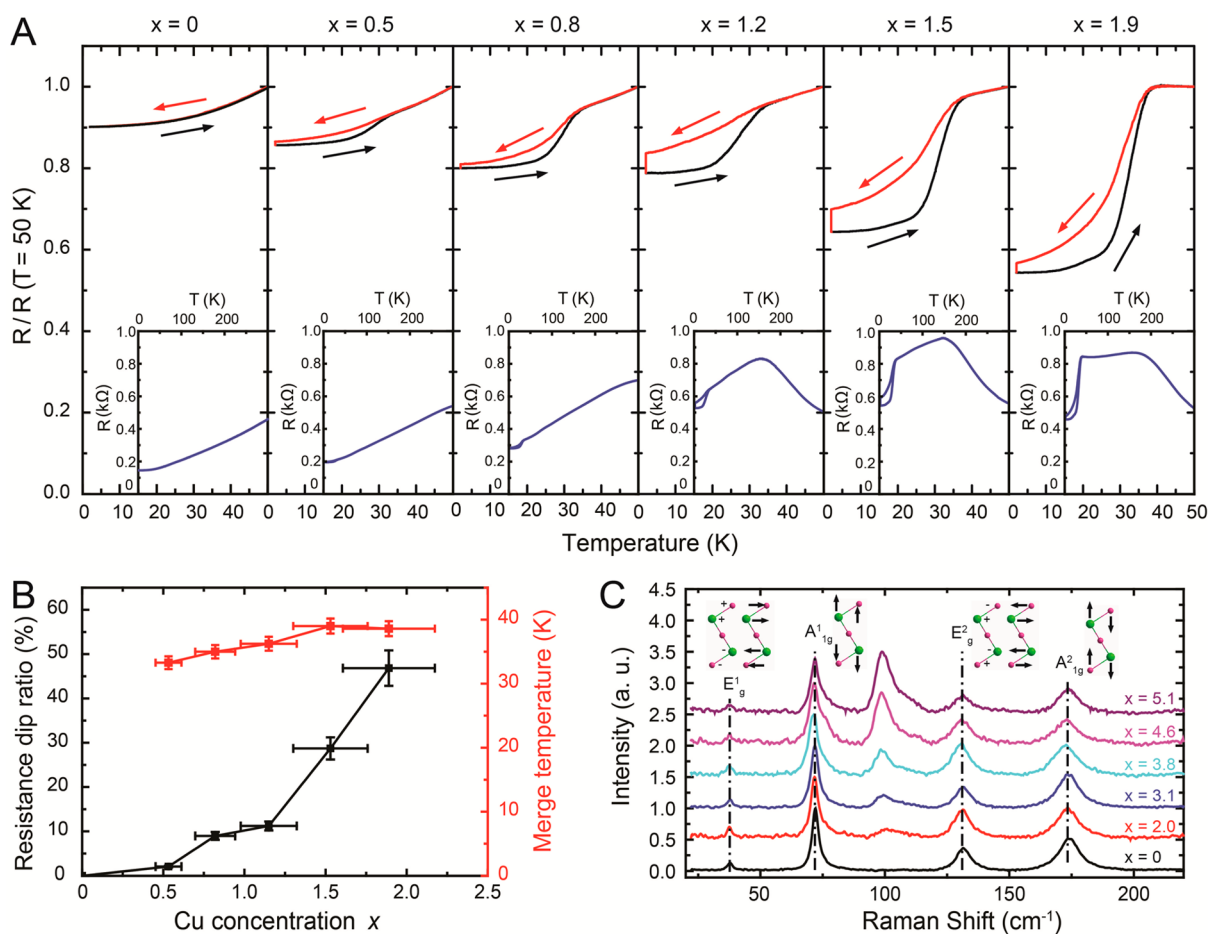


**Figure 3.** Low-temperature transport measurements and Raman spectroscopies of  $\text{Cu}_x\text{Bi}_2\text{Se}_3$  nanoribbons. (A) Normalized resistance  $R/R$  (50 K) versus temperature with Cu concentrations up to  $x = 1.9$ . The cooling (red) and warming (black) curves both uncover a resistance dip as well as a hysteresis behavior below 40 K with temperature varying rate at 1 K/min. The insets show whole resistance profiles from 300 to 2 K, displaying an insulator to metal transition at around 150 K for  $x = 1.2$  to 1.9. (B) The summary of resistance dip ratio and merge temperature where hysteresis disappears as a function of Cu concentration  $x$ . (C) Normalized Raman spectra with different Cu content from 0 to 5.1. The insets display the displacement patterns of  $E_g^1$ ,  $A_{1g}^1$ ,  $E_g^2$ , and  $A_{2g}^1$  phonon modes of a quintuple layer  $\text{Bi}_2\text{Se}_3$ .

the most energy favorable positions are the center of Se octahedrons in the van der Waals gap (the inset of Figure 1B). Since the octahedral centers are occupying the A, B, and C sites alternatively, it will form the same hexagonal diffraction pattern as Figure 2A until the maximum capacity  $\text{Cu}_{x=1}\text{Bi}_2\text{Se}_3$ . When more Cu atoms are intercalated, they will probably take the interstitial sites at the tetrahedral center of Se atoms in the gap (the inset of Figure 1B). Also, the Cu atoms may be further close-packed with the formation of Cu dimers or trimers in the van der Waals gap. If viewed from  $c$  direction, the Cu atoms are located at the triangular centers of Bi/Se atoms (Figure 2H), resulting in a diffraction pattern same as that shown in Figure 2B. As Cu concentration is further increased, it may induce a new interplanar stacking order. For instance, each quintuple layer,  $\text{Se}(1)\text{-Bi-Se}(2)\text{-Bi-Se}(1)$ , repetitively occupies the A-B-C-A-B sites, which gives rise to a Bi atom missing on C sites (Figure 2I) and enables the formation of  $\{1\bar{1}00\}$  hexagonal superlattice spots shown in Figure 2C. The simulated diffraction patterns of Figure 2G–I match the corresponding experimental results in Figure 2A–C.

The TEM-EDX spectroscopy was used to identify Cu concentration for each nanoribbon. As shown in Figure 2J, the EDX spectra normalized to the Se peak at 11.2 keV present an enhanced Cu contribution and nearly unchanged Bi/Se ratio as

$x$  is increased to 6.7. Because there is an overlap between  $\text{Cu-K}_\beta$  and  $\text{Ni-K}_\alpha$  (from TEM grids) peaks, we fitted double-peak curves and highlighted Cu contribution by solid colors. Moreover, the electron energy loss spectroscopy (EELS) was used to identify the oxidation states of Cu on the basis of the near-edge fine structure, such as  $L_3$  and  $L_2$  ratio (Figure 2K). Both these Cu intercalated nanoribbons show only broad edges, other than intense or sharp  $L_2$  and  $L_3$  edges in nonzero oxidation states ( $\text{Cu}^+$  or  $\text{Cu}^{2+}$ ),<sup>25,27</sup> indicating that the intercalated Cu atoms are in zerovalent state ( $\text{Cu}^0$ ).

After Cu intercalation, low-temperature transport measurements were performed on the  $\text{Bi}_2\text{Se}_3$  nanoribbons. Figure 3A presents normalized resistance curves [ $R/R$  (50 K)] as a function of temperature with different Cu concentrations up to  $x = 1.9$  with four-probe configuration (Figure S1). The Cu concentrations were determined by using scanning electron microscopy (SEM) EDX, as shown in Figure S6. It is necessary to announce that as-intercalated samples in our work did not show any superconductivity down to 2 K, consistent with that reported in previous literatures.<sup>33,34</sup> A probable reason is that the electrochemically intercalated Cu atoms occupy different sites compared with that in melt-growth bulk crystals and thus contribute different electron doping and coupling phonon modes. In addition, due to the nonuniformity of Cu

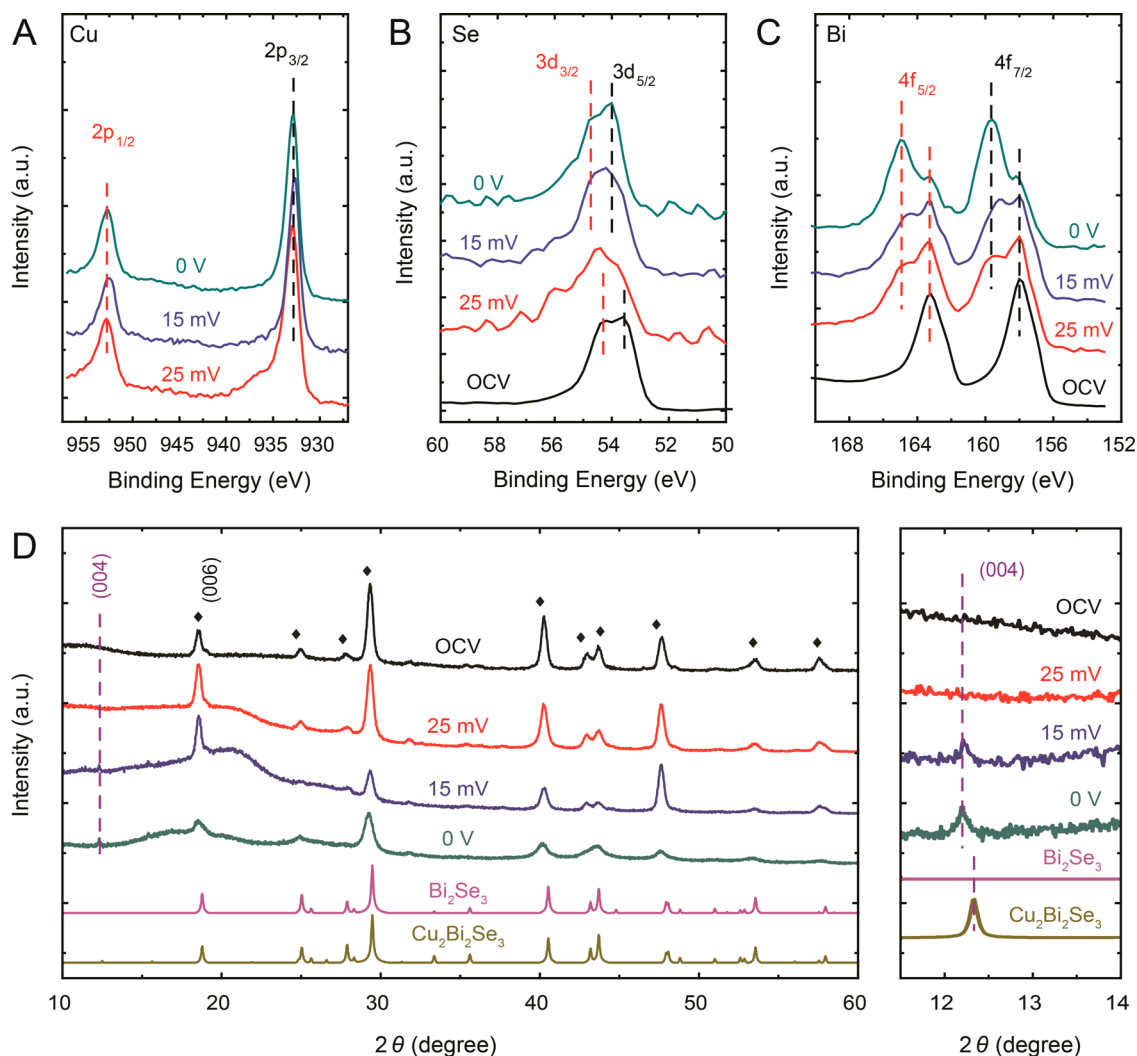


**Figure 4.** XPS and XRD spectra of  $\text{Cu}_x\text{Bi}_2\text{Se}_3$  nanoparticles with the cutoff voltages at OCV (41 mV), 25 mV, 15 mV, and 0 V, respectively. (A–C) XPS measurements for  $\text{Cu}_x\text{Bi}_2\text{Se}_3$  centered at Cu 2p (A), Se 3d (B), and Bi 4f (C) peaks. With increasing Cu concentration, Cu 2p peaks remain unchanged, while Se 3d and Bi 4f peaks shift to higher binding energies. (D) XRD patterns of Cu-intercalated  $\text{Bi}_2\text{Se}_3$ , as well as the standard X-ray diffraction of  $\text{Bi}_2\text{Se}_3$  (labeled as  $\blacklozenge$ , PDF 04-002-5483), and simulated  $\text{Cu}_2\text{Bi}_2\text{Se}_3$ .

concentration, the inner/outer part of each nanoribbon may be under-/overdoped, resulting in an elimination of superconducting regions.

Despite the absence of superconductivity, we still discovered more intriguing phenomena in our  $\text{Cu}_x\text{Bi}_2\text{Se}_3$  nanoribbons. As shown in Figure 3A, for pristine  $\text{Bi}_2\text{Se}_3$  ( $x = 0$ ) the resistance shows metallic behavior from room temperature down to 2 K due to electron doping mainly from Se vacancies.<sup>35,36</sup> When Cu atoms are intercalated to  $x = 0.5$  and 0.8, the overall resistance behavior remains metallic. Moreover, we uncovered a reinforced resistance dip starting from 35 K to the base temperature, accompanied with a hysteresis between the cooling and warming resistance curves. When Cu concentration is further increased from 1.2 to 1.9, the resistance curves show an insulating behavior cooling down from room temperature followed by an insulator–metal transition at around 150 K. Both the resistance dip ratios (see Figure S7 for extrapolation details) and hysteresis effect become more predominant compared to that with lower Cu concentrations as summarized in Figure 3B. In addition, the merge temperatures where the hysteresis disappears barely shift from 35 to 40 K. All these findings imply that a new phase may be formed at low

temperatures, and it should relate to some lattice reconstruction and behave as a resistance dip and hysteresis. For the samples with Cu concentrations higher than 1.9, both the resistance dip and hysteresis exist, though it is hard to obtain a systematic conclusion on the general tendency. Compared with the phase transition between commensurate and incommensurate charge density wave (CDW) in 1T-TaS<sub>2</sub>,<sup>12</sup> this new phase in  $\text{Cu}_x\text{Bi}_2\text{Se}_3$  possesses metallic resistance behavior other than the insulating CDW phase at low temperatures. In addition, similar hysteresis loop has been reported in VO<sub>2</sub> due to the crystallographic phase transition from tetragonal structure in a high-temperature metallic phase to a monoclinic structure in a low-temperature insulating phase.<sup>37,38</sup> Although more evidence is needed to further clarify the detailed structure of this low-temperature phase, we can still predict that intercalated Cu atoms play an essential role in conducting this phase transition.

Figure 3C shows normalized Raman spectra of  $\text{Bi}_2\text{Se}_3$  nanoribbons with a variety of intercalated Cu concentrations. Without Cu intercalation, the Raman spectrum of pristine  $\text{Bi}_2\text{Se}_3$  is consistent with that reported previously.<sup>39–41</sup> Four characteristic vibration modes  $E_{1g}^1$ ,  $A_{1g}^1$ ,  $E_{2g}^2$ , and  $A_{1g}^2$  are located at  $\sim 37$ ,  $\sim 72$ ,  $\sim 131$ , and  $\sim 174$   $\text{cm}^{-1}$ , respectively. The

inset illustrates the schematics of these four Raman-active modes in a  $\text{Bi}_2\text{Se}_3$  quintuple layer. When Cu atoms are introduced, the original four modes of pristine  $\text{Bi}_2\text{Se}_3$  are not shifted at all. However, a new vibration mode appears at  $\sim 99\text{ cm}^{-1}$  with gradually strengthened intensity as Cu concentration is increased. Since this new mode has no relationship with Cu precipitates or  $[\text{Cu}(\text{CH}_3\text{CN})_4]\text{PF}_6$  salts (Figure S8), it should arise from the formation of extra bonding between Cu and Bi/Se atoms. Although it is hard to identify the exact vibration model, the discovery itself for the first time in Cu intercalated  $\text{Bi}_2\text{Se}_3$  nanoribbons is still attractive.

To take full advantage of electrochemical reaction, coulometric method is adopted to control the intercalant concentration in a more accurate and controllable way. Because the mass loading of  $\text{Bi}_2\text{Se}_3$  nanoribbons on the substrate is too low, the WE was replaced by  $\text{Bi}_2\text{Se}_3$  nanoparticles coated on Pt plate (Figure S3). The electrochemical intercalation was carried out by the galvanostatic method in a two-electrode arrangement at a current of 400 nA. In contrast to the  $\text{Bi}_2\text{Se}_3$  nanoribbons (Figure 1B), this  $\text{Bi}_2\text{Se}_3$ -nanoparticle electrode shows an open circuit voltage (OCV) of 41 mV and a gently sloping curve for Cu electrochemical intercalation, after 40 h followed by a flat voltage plateau for Cu metal deposition (Figure S4). This sloping curve is probably due to the reduced surface to volume ratio or inhomogeneity in the grain size. Nevertheless, the long-lasting positive voltage offers us enough capability to control the electrochemical reaction time; thus, the Cu concentration  $x$  could be calculated based on the accumulated electron quantity (see Supporting Information for calculation details). At various cutoff potentials, 25 mV, 15 mV, and 0 V, the Cu concentration  $x$  was calculated to be 0.55, 1.02, and 1.51 by using the coulometric method. Meanwhile, the gravimetric and XPS analysis were also performed to evaluate the Cu concentration and displayed consistent results (see Table 1 in Supporting Information). The coincidence of these three methods indicates that it is practical to control the Cu concentration by means of electrochemical method in a more manageable and accurate way.

At the meantime, further analysis of XPS data provides more information on investigating the chemical states of Cu, Se, and Bi as well as the Cu concentrations at various potentials. All the Cu 2p XPS spectra of the Cu-intercalated samples (Figure 4A) display that the  $2\text{p}_{3/2}$  and  $2\text{p}_{1/2}$  peaks are located at 932.84 and 952.74 eV without satellite peaks, characteristic of the absence of nonzerovalent state ( $\text{Cu}^+$  or  $\text{Cu}^{2+}$ ).<sup>25</sup> For the pristine  $\text{Bi}_2\text{Se}_3$  case at OCV, the Se  $3\text{d}_{5/2}$  and Bi  $4\text{f}_{7/2}$  peaks center at 53.6 and 158.0 eV in Figure 4B,C, identifying the reduction state of  $\text{Se}^{2-}$  and the oxidation state of  $\text{Bi}^{3+}$ , respectively. With increasing the intercalated Cu atoms, both of the Se 3d and Bi 4f peaks shift to higher binding energy, indicating that the electron clouds around them are moved away from the nucleus. In addition, we have performed first-principles calculation to further study the influence of Cu intercalation on the chemical states of Se and Bi. Compared with the pristine  $\text{Bi}_2\text{Se}_3$ , both the isosurfaces of Se and Bi atoms expand after Cu atom intercalation (Figure S9). It denotes that the electron clouds surrounding Se and Bi atoms move to Cu atoms, resulting in more electron doping to the van der Waals gap.

XRD diffractogram of  $\text{Bi}_2\text{Se}_3$  for Cu intercalation are shown in Figure 4D, the top black line reveals the characteristic diffraction peaks of the pristine  $\text{Bi}_2\text{Se}_3$  in which no diffraction peak of (004) crystal plane can be detected. With increasing Cu intercalants, the (004) diffraction peaks present in the samples

with cutoff potential at 15 mV and 0 V, respectively (right panel in Figure 4D). In addition, the (004) diffraction peaks shift toward a lower angle compared with the simulated results of  $\text{Cu}_2\text{Bi}_2\text{Se}_3$  by using the same crystal parameters as  $\text{Bi}_2\text{Se}_3$ , indicating that the van der Waals gap has been increased owing to the intercalation of Cu atoms.

In summary, this investigation offers an electrochemical intercalation methodology to readily intercalate zerovalent Cu atoms into nanoscale  $\text{Bi}_2\text{Se}_3$  without disrupting the host lattice. Moreover, it has been implemented to control the Cu concentrations accurately by using coulometric strategy. For the first time, we uncovered an unconventional resistance dip accompanied by a hysteresis behavior below 40 K and new vibration peaks in the Raman spectra. We foresee the potential impact of this methodology in establishing fundamentally new and unexpected physical behaviors as well as a new method for possible atomic energy storage or catalytic material applications. This methodology appears to be general and may be extended to intercalate other zerovalent metals into more general 2D layered nanomaterials.

## ■ ASSOCIATED CONTENT

### Supporting Information

The Supporting Information is available free of charge on the ACS Publications website at DOI: 10.1021/acs.nanolett.6b05062.

Growth of  $\text{Bi}_2\text{Se}_3$  nanowire, details about the electrochemical setup, device fabrication, low-temperature transport measurements, TEM imaging, XRD, XPS, EDX, and Raman spectroscopy, more discussions and characterizations of Cu intercalated  $\text{Bi}_2\text{Se}_3$  nanoparticles, analysis methods of Cu concentrations, other supporting figures (PDF)

## ■ AUTHOR INFORMATION

### Corresponding Author

\*E-mail: yicui@stanford.edu.

### ORCID

Jinsong Zhang: 0000-0002-3601-4995

### Author Contributions

J.Z. and J.S. contributed equally to this work. Y.C., J. Z., and J.S. conceived and designed the experiments. J.Z. performed  $\text{Bi}_2\text{Se}_3$  nanoribbon growth, device fabrication, Raman spectroscopy, and low-temperature transport measurements. J.Z. and J.S. carried out the electrochemical intercalation. J.S. did the XPS, XRD characterizations, and first-principle simulations. Y.L. and J.S. performed TEM imaging, EELS, and EDX. F.S. carried out the EDX in SEM. All authors discussed the results and commented on the manuscript.

### Notes

The authors declare no competing financial interest.

## ■ ACKNOWLEDGMENTS

We are grateful to Yi Yu for useful discussions on TEM characterizations and Kai Liu for optical spectroscopy measurements. This work was supported by the Department of Energy, Office of Basic Energy Sciences, Division of Materials Sciences and Engineering, under contract DE-AC02-76SF00515.

## ■ REFERENCES

- (1) Castro Neto, A. H.; Guinea, F.; Peres, N. M. R.; Novoselov, K. S.; Geim, A. K. *Rev. Mod. Phys.* **2009**, *81* (1), 109–162.
- (2) Sun, Z.; Martinez, A.; Wang, F. *Nat. Photonics* **2016**, *10* (4), 227–238.
- (3) Butler, S. Z.; Hollen, S. M.; Cao, L.; Cui, Y.; Gupta, J. A.; Gutiérrez, H. R.; Heinz, T. F.; Hong, S. S.; Huang, J.; Ismach, A. F.; Johnston-Halperin, E.; Kuno, M.; Plashnitsa, V. V.; Robinson, R. D.; Ruoff, R. S.; Salahuddin, S.; Shan, J.; Shi, L.; Spencer, M. G.; Terrones, M.; Windl, W.; Goldberger, J. E. *ACS Nano* **2013**, *7* (4), 2898–2926.
- (4) Koski, K. J.; Cui, Y. *ACS Nano* **2013**, *7* (5), 3739–3743.
- (5) Wang, Q. H.; Kalantar-Zadeh, K.; Kis, A.; Coleman, J. N.; Strano, M. S. *Nat. Nanotechnol.* **2012**, *7* (11), 699–712.
- (6) Wan, J.; Lacey, S. D.; Dai, J.; Bao, W.; Fuhrer, M. S.; Hu, L. *Chem. Soc. Rev.* **2016**, *45* (24), 6742–6765.
- (7) Schöllhorn, R. Materials and Models: Faces of Intercalation Chemistry. In *Progress in Intercalation Research*; Müller-Warmuth, W., Schöllhorn, R., Eds.; Kluwer: Dordrecht, The Netherlands, 1994; Vol. 17, pp 1–81.
- (8) Friend, R. H.; Yoffe, A. D. *Adv. Phys.* **1987**, *36* (1), 1–94.
- (9) Dresselhaus, M. S.; Dresselhaus, G. *Adv. Phys.* **2002**, *51* (1), 1–186.
- (10) Liang, W. Y. Electronic Properties of Transition Metal Dichalcogenides and their Intercalation Complexes. In *Intercalation in Layered Materials*; Dresselhaus, M. S., Ed.; Plenum Press: New York, 1986; Vol. 148, pp 31–74.
- (11) Pamplin, B. R. Introduction to Crystal Growth Methods. In *Crystal Growth*; Pamplin, B. R., Ed.; Pergamon Press: Oxford, 1980; Vol. 16, pp 1–21.
- (12) Yu, Y.; Yang, F.; Lu, X. F.; Yan, Y. J.; Cho, Y.-H.; Ma, L.; Niu, X.; Kim, S.; Son, Y.-W.; Feng, D.; Li, S.; Cheong, S.-W.; Chen, X. H.; Zhang, Y. *Nat. Nanotechnol.* **2015**, *10* (3), 270–276.
- (13) Bao, W.; Wan, J.; Han, X.; Cai, X.; Zhu, H.; Kim, D.; Ma, D.; Xu, Y.; Munday, J. N.; Drew, H. D.; Fuhrer, M. S.; Hu, L. *Nat. Commun.* **2014**, *5*, 4224.
- (14) Xiong, F.; Wang, H.; Liu, X.; Sun, J.; Brongersma, M.; Pop, E.; Cui, Y. *Nano Lett.* **2015**, *15* (10), 6777–6784.
- (15) Thenuwar, A. C.; Shumlas, S. L.; Attanayake, N. H.; Cerkez, E. B.; McKendry, I. G.; Frazer, L.; Borguet, E.; Kang, Q.; Zdilla, M. J.; Sun, J.; Strongin, D. R. *Langmuir* **2015**, *31* (46), 12807–12813.
- (16) Kapper, R.; Voiry, D.; Yalcin, S. E.; Branch, B.; Gupta, G.; Mohite, A. D.; Chhowalla, M. *Nat. Mater.* **2014**, *13* (12), 1128–1134.
- (17) Sun, J.; Lee, H.-W.; Pasta, M.; Yuan, H.; Zheng, G.; Sun, Y.; Li, Y.; Cui, Y. *Nat. Nanotechnol.* **2015**, *10* (11), 980–985.
- (18) Morosan, E.; Zandbergen, H. W.; Dennis, B. S.; Bos, J. W. G.; Onose, Y.; Klimczuk, T.; Ramirez, A. P.; Ong, N. P.; Cava, R. J. *Nat. Phys.* **2006**, *2* (8), 544–550.
- (19) Li, T.; Liu, Y.-H.; Chitara, B.; Goldberger, J. E. *J. Am. Chem. Soc.* **2014**, *136* (8), 2986–2989.
- (20) Hor, Y. S.; Williams, A. J.; Checkelsky, J. G.; Roushan, P.; Seo, J.; Xu, Q.; Zandbergen, H. W.; Yazdani, A.; Ong, N. P.; Cava, R. J. *Phys. Rev. Lett.* **2010**, *104* (5), 057001.
- (21) Kriener, M.; Segawa, K.; Ren, Z.; Sasaki, S.; Ando, Y. *Phys. Rev. Lett.* **2011**, *106* (12), 127004.
- (22) Wray, L. A.; Xu, S.-Y.; Xia, Y.; Hor, Y. S.; Qian, D.; Fedorov, A. V.; Lin, H.; Bansil, A.; Cava, R. J.; Hasan, M. Z. *Nat. Phys.* **2010**, *6* (11), 855–859.
- (23) Wang, Y.-L.; Xu, Y.; Jiang, Y.-P.; Liu, J.-W.; Chang, C.-Z.; Chen, M.; Li, Z.; Song, C.-L.; Wang, L.-L.; He, K.; Chen, X.; Duan, W.-H.; Xue, Q.-K.; Ma, X.-C. *Phys. Rev. B: Condens. Matter Mater. Phys.* **2011**, *84* (7), 075335.
- (24) Kondo, R.; Yoshinaka, T.; Imai, Y.; Maeda, A. *J. Phys. Soc. Jpn.* **2013**, *82* (6), 063702.
- (25) Koski, K. J.; Cha, J. J.; Reed, B. W.; Wessells, C. D.; Kong, D.; Cui, Y. *J. Am. Chem. Soc.* **2012**, *134* (18), 7584–7587.
- (26) Koski, K. J.; Wessells, C. D.; Reed, B. W.; Cha, J. J.; Kong, D.; Cui, Y. *J. Am. Chem. Soc.* **2012**, *134* (33), 13773–13779.
- (27) Motter, J. P.; Koski, K. J.; Cui, Y. *Chem. Mater.* **2014**, *26* (7), 2313–2317.
- (28) Chen, K. P.; Chung, F. R.; Wang, M.; Koski, K. J. *J. Am. Chem. Soc.* **2015**, *137* (16), 5431–5437.
- (29) Zhang, H.; Liu, C.-X.; Qi, X.-L.; Dai, X.; Fang, Z.; Zhang, S.-C. *Nat. Phys.* **2009**, *5* (6), 438–442.
- (30) Zhang, Y.; He, K.; Chang, C.-Z.; Song, C.-L.; Wang, L.-L.; Chen, X.; Jia, J.-F.; Fang, Z.; Dai, X.; Shan, W.-Y.; Shen, S.-Q.; Niu, Q.; Qi, X.-L.; Zhang, S.-C.; Ma, X.-C.; Xue, Q.-K. *Nat. Phys.* **2010**, *6* (8), 584–588.
- (31) Xia, Y.; Qian, D.; Hsieh, D.; Wray, L.; Pal, A.; Lin, H.; Bansil, A.; Grauer, D.; Hor, Y. S.; Cava, R. J.; Hasan, M. Z. *Nat. Phys.* **2009**, *5* (6), 398–402.
- (32) Shannon, R. *Acta Crystallogr., Sect. A: Cryst. Phys., Diffr., Theor. Gen. Crystallogr.* **1976**, *32* (5), 751–767.
- (33) Kriener, M.; Segawa, K.; Ren, Z.; Sasaki, S.; Wada, S.; Kuwabata, S.; Ando, Y. *Phys. Rev. B: Condens. Matter Mater. Phys.* **2011**, *84* (5), 054513.
- (34) Shirasawa, T.; Sugiki, M.; Hirahara, T.; Aitani, M.; Shirai, T.; Hasegawa, S.; Takahashi, T. *Phys. Rev. B: Condens. Matter Mater. Phys.* **2014**, *89* (19), 195311.
- (35) Peng, H.; Lai, K.; Kong, D.; Meister, S.; Chen, Y.; Qi, X.-L.; Zhang, S.-C.; Shen, Z.-X.; Cui, Y. *Nat. Mater.* **2010**, *9* (3), 225–229.
- (36) Kong, D.; Randel, J. C.; Peng, H.; Cha, J. J.; Meister, S.; Lai, K.; Chen, Y.; Shen, Z.-X.; Manoharan, H. C.; Cui, Y. *Nano Lett.* **2010**, *10* (1), 329–333.
- (37) Jeromin, H.; Picard, F.; Vincent, D. *Opt. Eng.* **1993**, *32* (9), 2092–2099.
- (38) Choi, H. S.; Ahn, J. S.; Jung, J. H.; Noh, T. W.; Kim, D. H. *Phys. Rev. B: Condens. Matter Mater. Phys.* **1996**, *54* (7), 4621–4628.
- (39) Zhang, J.; Peng, Z.; Soni, A.; Zhao, Y.; Xiong, Y.; Peng, B.; Wang, J.; Dresselhaus, M. S.; Xiong, Q. *Nano Lett.* **2011**, *11* (6), 2407–2414.
- (40) Shahil, K. M. F.; Hossain, M. Z.; Goyal, V.; Balandin, A. A. *J. Appl. Phys.* **2012**, *111* (5), 054305.
- (41) Richter, W.; Becker, C. R. *Phys. Status Solidi B* **1977**, *84* (2), 619–628.